

Physical properties of carbonate fault rocks, fucino basin (Central Italy): implications for fault seal in platform carbonates

F. AGOSTA¹, M. PRASAD^{2*} AND A. AYDIN¹

¹*Rock Fracture Project, Department of Geological and Environmental Sciences and* ²*Geophysics Department, Stanford University, Stanford, CA, USA*

ABSTRACT

We documented the porosity, permeability, pore geometry, pore type, textural anisotropy, and capillary pressure of carbonate rock samples collected along basin-bounding normal faults in central Italy. The study samples consist of one Mesozoic platform carbonate host rock with low porosity and permeability, four fractured host rocks of the damage zones, and four fault rocks of the fault cores. The four fractured samples have high secondary porosity, due to elongated, connected, soft pores that provide fluid pathways in the damage zone. We modeled this zone as an elastic cracked medium, and used the Budiansky–O’Connell correlation to compute its permeability from the measured elastic moduli. This correlation can be applied only to fractured rocks with large secondary porosity and high-aspect ratio pores. The four fault rock samples are made up of survivor clasts embedded in fine carbonate matrices and cements with sub-spherical, stiff pores. The low porosity and permeability of these rocks, and their high values of capillary pressure, are consistent with the fault core sealing as much as 77 and 140 m of gas and oil columns, respectively. We modeled the fault core as a granular medium, and used the Kozeny–Carmen correlation, assigning the value of 5 to the Kozeny constant, to compute its permeability from the measured porosities and pore radii. The permeability structure of the normal faults is composed of two main units with unique hydraulic characteristics: a granular fault core that acts as a seal to cross-fault fluid flow, and an elastic cracked damage zone that surrounds the core and forms a conduit for fluid flow. Transient pathways for along-fault fluid flow may form in the fault core during seismic faulting due to the formation of opening-mode fractures within the cemented fault rocks.

Key words: fault permeability structure, fault rocks, normal fault, platform carbonates, pore structure, sealing potential

Received 9 November 2005; accepted 26 June 2006

Corresponding author: Fabrizio Agosta, Dipartimento di Scienze della Terra, Università di Camerino, via Gentile III da Varano, 62032 Camerino (Mc), Italy.

Email: fabrizio_agosta@hotmail.com. Tel: +39 334 910 4541

*Present address: Earth Science Department, Università di Camerino, Italy.

Geofluids (2007) 7, 19–32

INTRODUCTION

Faults evolve by formation and interaction of structural elements that compose a core of highly deformed fault rocks sandwiched between less deformed rocks (Sibson 1977; Chester & Logan 1986; Cello 2000). The fault core is a narrow zone that forms, more commonly, between major slip surfaces; this is the site of comminution, dissolution/precipitation, mineral reactions, and other mechanical and chemical processes that effectively destroy the fabric of the

original host rock. The damage zone flanks the fault core, and is a wider zone of deformation with numerous fractures and small faults that do not completely obliterate the host rock fabric. Both fault core and damage zone are encompassed by the host rock, which is characterized by background tectonic structures due to previous deformation. Understanding of faulting processes and their products, such as core and damage zone composition, petrophysics, spatial distribution, as well the characterization of their geometry, diagenesis, and mechanical proper-

ties are crucial to building predictive models of fault zone architecture and fluid flow pathways in faulted and fractured reservoirs (Caine *et al.* 1996; Aydin 2000).

Several models of fault permeability have been proposed for faults in clastic and crystalline rocks (Scholz 1990; Antonellini & Aydin 1994; Bruhn *et al.* 1994; Caine & Forster 1999; Rawling *et al.* 2001; Flodin *et al.* 2005). These models, however, are not completely applicable to faults in carbonate rocks because of their unique deformation mechanisms (Willemsse *et al.* 1997; Kelly *et al.* 1998; Mollena & Antonellini 1999; Salvini *et al.* 1999; Graham *et al.* 2003; Agosta & Aydin 2006; Tondi *et al.* 2006), and peculiar pore types, such as vugs, molds, fractures, and channels (Wang 1997; Lucia 1999). Furthermore, there are few data published on the petrophysical properties of carbonate fault rocks to develop a reliable model of fault permeability in carbonate reservoirs. In order to fill this gap, we present the results of optical microscopy, porosity, permeability, ultrasonic, and mercury-injection analyses on samples of intact and deformed carbonates collected in the footwall of normal faults that border the east side of the Fucino continental basin, central Italy. This basin, characterized by a half-graben structure, is filled with Late Pliocene–Holocene fluvio-lacustrine sediments (Galadini & Messina 1994; Cavinato *et al.* 2002). The host rock sample, collected outside of the normal fault zones, consists of a Mesozoic platform carbonate with low porosity and permeability. The deformed samples comprise fractured host rocks of the damage zones, and matrix- and cement-supported fault rock samples of the cores that will be referred as uncemented and cemented fault rocks, respectively.

In this paper we first determine the porosity, permeability, pore geometry, and pore type of the nine rock samples.

Then, we assess the textural anisotropy, sealing potential, and pore radii of the four fault rock samples collected from the cores. Based on the results of these analyses, we model the fault cores as a granular media and the damage zones as an elastic cracked media to compute their permeability using the Kozeny–Carmen (Tiab & Donaldson 1996) and Budiansky–O’Connell correlations (Budiansky & O’Connell 1976), respectively. Finally, we compare the calculated values of permeability with the measured values to test the validity of these correlations to normal fault zones in platform carbonates.

INTERNAL STRUCTURE OF THE NORMAL FAULTS

The normal faults that border the Fucino basin strike N110–140E and dip 50° to 65°SW (Fig. 1). These faults crosscut the Apenninic fold-and-thrust belt to depths of 10–15 km (Ghisetti & Vezzani 1999, and references therein), and juxtapose the basin filling sediments against the Upper Jurassic–Lower Cretaceous, platform carbonates of the Lazio-Abruzzi tectonic unit (Vezzani & Ghisetti 1998). The platform carbonates are about 1200 m thick, exhumed from more than 1 km (Ghisetti & Vezzani 1999), and unconformably overlain by 100s of meters thick Middle Miocene grainstones and Messinian flysch.

The individual segments of the basin-bounding normal faults are several kilometers long (Fig. 2), have as much as 0.6 km of throw (Cavinato *et al.* 2002), and last ruptured during the Ms = 7.0 Avezzano earthquake of 1915 (Boschi *et al.* 1997). Focal mechanism solutions of the Avezzano earthquake suggest oblique slip dominated by a normal component (Gasparini *et al.* 1985; Basili & Valen-

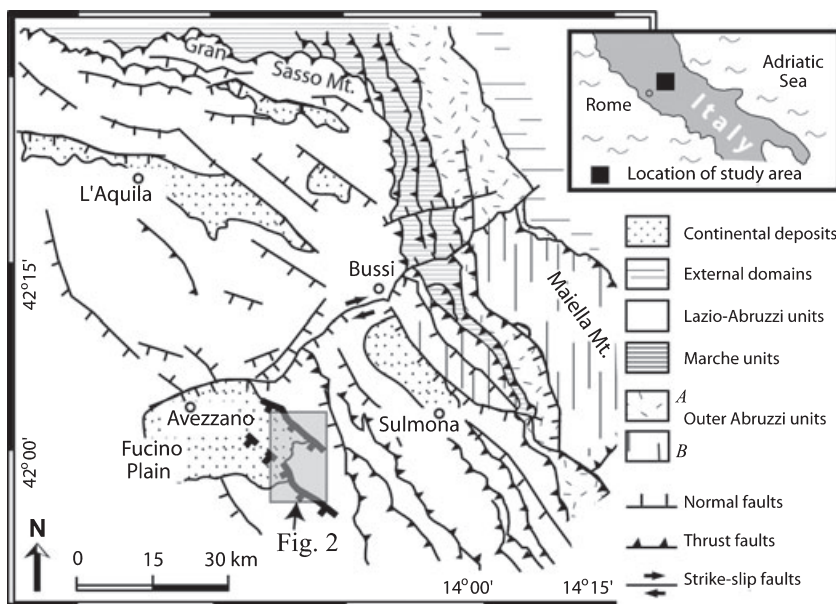


Fig. 1. Simplified regional map of the Abruzzo region, central Italy (after Vezzani & Ghisetti 1998). The Lazio-Abruzzi and Outer Abruzzi-B units comprise platform carbonates, whereas the Marche and Outer Abruzzi-A units are clastic rocks. The shaded area denotes the study area along the southeast side of the Fucino basin, which is bounded by two major normal faults shown in bold.

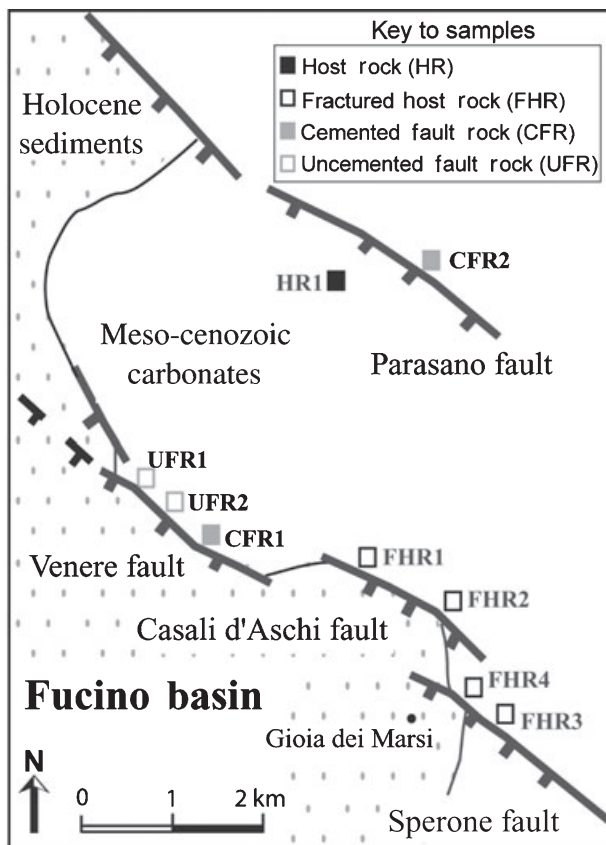


Fig. 2. Simplified structural map of the southeast side of the Fucino basin showing the trace of the basin-bounding, major normal fault segments. The hatchmarks indicate the fault hangingwall sides, the squares the sample locations with adjacent sample names and numbers.

side 1991), whereas trench investigation in selected localities shows pure normal faulting (Micchetti *et al.* 1996). Over the entire Fucino area, minor right-lateral slip and an average slip rate of $0.4\text{--}1.0\text{ mm year}^{-1}$ have been documented by the analysis of widespread fault scarps (Piccardi *et al.* 1999).

The background structures of the platform carbonates host rock consist of closing mode (pressure solution seams), opening mode (joints and veins), and shearing mode fractures (primarily sheared seams) that formed during burial diagenesis and Oligo-Pliocene contraction of the Apennine belt (Agosta & Aydin 2006). Internal units of the normal faults include deformed continental sediments in the hangingwall, major slip surfaces coated with calcite cement, and up to 1 m thick fault rocks of the core and tens of meters thick fractured and fragmented carbonates of the damage zone in the footwall (Fig. 3). The fluvial and lacustrine sediments in the hangingwall are widely deformed in the vicinity of the faults; in the study area, the sediments are brecciated and cemented within 1 m of the major slip surfaces. Centimeters thick slivers of sediments and slope scree are often sheared and accreted into the

fault footwall due to the basinward migration of these slip surfaces.

The internal structure of the normal fault zones has been studied in detail along the Venere fault zone, a detailed cross-section of which is presented in Agosta & Aydin (2006). Based on their length and throw, we recognized three different fault strands within the Venere fault zone. The first strand has an offset of a few hundred meters, juxtaposes the Quaternary sediments against the Mesozoic carbonates, and is associated with an up to 1 m thick fault core comprised of fault rocks and major slip surfaces. Both second- and third-order fault strands are within the damage zone of the Venere fault zone. The second-order fault strands are characterized by several tens of meters offset, and bound slivers of platform carbonate rocks having different deformation intensity and dip angles. The internal make up of these faults consists of several centimeters thick cemented and uncemented, comminuted protocataclite (*sensu* Sibson 1977), flanked by a few meters thickness of fragmented carbonate rocks. The third-order faults, present within the slivers bounded by the second-order faults, have an offset range on the order of a few centimeters to several meters. The internal structure of the third-order faults is made up of fragmented and brecciated carbonate rocks and, sporadically, millimeter and centimeter thick comminuted fault rocks.

The samples of matrix- and cement-supported fault rocks were collected along the Parasano and Venere fault zones, which are bounded by highly fragmented and pulverized carbonate host rocks that are part of the fault damage zones. The matrix-supported fault rocks, which are continuous along the mapped outcrops of three fault zones, are made up of survivor clasts embedded in very fine-grained calcite matrix. The centimeter thick cement-supported fault rocks localize near the major slip surfaces. These rocks comprise low-Mg calcite cement that precipitated from an original meteoric fluid that mixed with the local groundwater and/or soil before it was channeled along the major slip surfaces of the fault cores (Ghisetti *et al.* 2001; Agosta & Kirschner 2003).

The samples of fractured host rocks were collected in the fractured carbonate host rocks of the damage zones of the Casali d'Aschi and Sperone fault zones, which contain several sets of opening mode (joints and veins), closing mode (pressure solution seams), and shearing mode fractures (sheared seams and sheared joints/veins), as reported by Agosta & Aydin (2006).

EXPERIMENTAL PROCEDURE

In order to characterize the mineralogy, petrophysics, and capillary pressure of the main fault components, we analyzed one platform carbonate host rock (HR1), four fractured host rocks (FHR1–4) of the damage zones, two

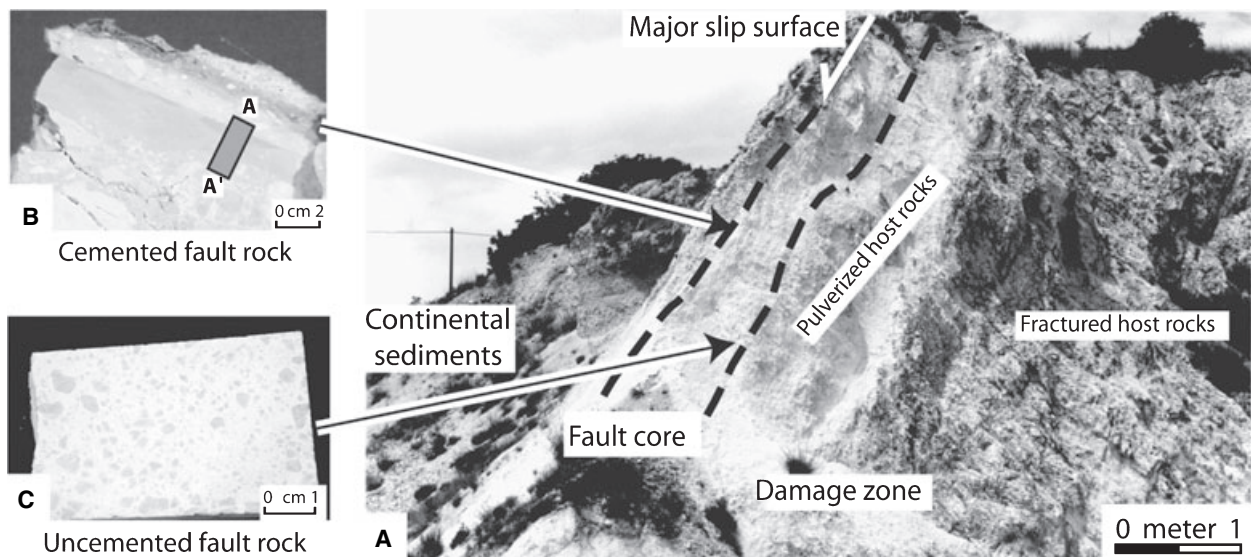


Fig. 3. (A) Cross-sectional photographic view of the Venere fault, which juxtaposes the continental sediments of the hangingwall with deformed carbonates. In the footwall the fault zone comprises fractured and pulverized host rocks of the damage zone, and a fault core of both matrix- and cement-supported fault rocks that are referred as (B) cemented and (C) uncemented fault rocks, respectively. The rectangle showing A to A' in Fig. 3B marks the location of the thin-sections shown in Fig. 5.

cemented (CFR1 and 2), and two uncemented fault rocks (UFR1 and 2) of the fault cores. The nine samples were selected from a suite of 55 that were collected along the normal faults that border the southeast part of the basin. These samples, representative of the internal units of the faults, were chosen based on their lack of weathering. Visual inspection in the field indicates that these units are continuous along the faults except at their peripheries. The sample locations are shown in Fig. 2. The highly fragmented and pulverized carbonate rocks of the damage zone, which are broken into millimeter to centimeter thick fragments, could not be sampled for thin-sectioning and laboratory analyses. The host rock sample was collected several hundreds of meters from the main fault segments, in an area where the carbonates are characterized by background values of deformation. The four fractured host rock samples, collected along the Casali d'Aschi and Sperone fault segments, and the two uncemented fault rocks, collected along the Venere fault, were sampled at various distances from the major slip surfaces. The cemented fault rock samples were collected along the major slip surfaces of the Venere and Parasano faults.

Sampling in the field was carried out after removing the first 10–15 cm of weathered outcrop material. Each sample was cut along two orthogonal directions, respectively, parallel and perpendicular to the major slip surfaces, for thin-sectioning, and then analyzed under a cross-polarized, transmitted light optical microscope to characterize both mineralogy and diagenetic history. Then, the samples were drilled to obtain cylindrical cores 3–5 cm long, and

2.54 cm in diameter for porosity, permeability, and ultrasonic analyses. The faces of the cylindrical core plugs are parallel to within 100 μm . Samples CFR1 and UFR1 were drilled orthogonal to the orientation of the major slip surfaces, whereas all the other fault-related samples (CFR2, UFR2, FHR1–4) were cut parallel to them. The host rock sample was cut parallel to the bedding. Cuttings of the hand specimens of uncemented fault rock recovered from the thin-sectioning were used for mercury-injection capillary tests.

LABORATORY ANALYSES AND RESULTS

We used a Helium porosimeter that is based on the Boyle's Law double-cell method to measure bulk and grain densities and to calculate the porosity of the nine samples. The P- and S-wave velocity (V_p and V_s , respectively) were measured using the pulse transmission technique (Prasad *et al.* 1999; Vanorio *et al.* 2002; Prasad & Nur 2003) at increasing confining pressures (P_c) up to 25 MPa (samples CFR2 and FHR2) and 50 MPa (all the other samples). Commercial laboratories performed both permeability and high-pressure mercury-injection capillary tests. All laboratory results are reported in Table 1 and are discussed in detail below.

Mineralogy

The platform carbonate host rock is a boundstone made up of calcite, a small amount of dolomite, and dark lime

Table 1 Results of porosity, permeability, and ultrasonic analyses performed on the nine samples, including values of permeability calculated for the uncemented fault rocks using the Kozeny–Carmen correlation and for the fractured host rocks using the Budiansky–O’Connell correlation.

Rock type	Sample name	Porosity (%)	Klinkenberg permeability (m ²)	P_c (MPa)	V_p (km sec ⁻¹)	V_s (km sec ⁻¹)	K (GPa)	μ (GPa)	ν	Calculated permeability (m ²)
Host rock	HR1	0.8	6.77×10^{-19}	5	6.28	3.19	70.26	27.59	0.33	—
Fractured host rock	FHR1	3	7.72×10^{-14}	5.1	5.63	3.01	51.93	23.99	0.3	8.17×10^{-15} 2.28×10^{-14} 6.27×10^{-14}
Fractured host rock	FHR2	1.6	—	5.1	5.73	3.11	46.26	22.49	0.29	—
Fractured host rock	FHR3	1.3	2.61×10^{-16}	4.9	6	3.07	61.52	24.79	0.32	7.12×10^{-15} 1.97×10^{-14} 5.34×10^{-14}
Fractured host rock	FHR4	1.27	1.45×10^{-17}	6	6.03	3.17	62.56	27.27	0.31	7.64×10^{-15} 2.12×10^{-14} 5.81×10^{-14}
Cemented fault rock	CFR1	0.6	$<9.67 \times 10^{-20}$	4.9	6.43	3.22	74.79	28.06	0.33	—
Cemented fault rock	CFR2	0.56	$<9.67 \times 10^{-20}$	6.6	6.56	3.14	79.03	26.01	0.35	—
Uncemented fault rock	UFR1	5.4	1.35×10^{-16}	4.9	6.03	2.9	67.22	22.54	0.35	3.87×10^{-16}
Uncemented fault rock	UFR2	2.5	1.16×10^{-16}	4.8	5.79	2.97	56.15	22.78	0.32	2.22×10^{-16}

The three different values of calculated permeability for the fractured host rocks are obtained by assuming average fracture orientations relative to the long axis of the core plugs ranging from normal, to diagonal, to parallel. The parameters listed include P-wave velocity (V_p), S-wave velocity (V_s), bulk modulus (K), shear modulus (μ), and Poisson’s ratio (ν) measured during increasing confining pressure (P_c).

mud that fills the pore space (Fig. 4A). The boundstone host rock underwent two main diagenetic phases: an early marine diagenesis and a late burial diagenesis. The former phase started soon after deposition with formation of micritic crusts around fossils thereby binding the rock. These crusts provided the substrate on top of which acicular cements (originally aragonite, now calcite) and ulterior micritic crusts formed. Marine diagenesis also involved the re-crystallization of lamellar calcite within the fossils, and formation of the lime mud from original calcareous algae. The burial diagenesis was responsible for the precipitation of small amounts of sparry calcite within the pore space and formation of bed-parallel pressure solution seams visible at both meso- and micro-scale.

The fractured host rocks of the damage zones are interlaced by fractures and faults. Microscopically, these rocks preserve some of the original sedimentary fabric; the fractures consist of different sets of pressure solution seams and joints that are filled with epoxy in the microphotograph of Fig. 4B. The fractured samples also contain several sets of veins filled with calcite and chlorite. The fault rocks, which are comminuted and fragmented at micro-scale by cataclastic deformation, are made up of angular-to-subrounded survivor clasts of calcite, and rare dolomite, embedded in fine calcite matrices (Fig. 4C) and low-Mg calcite cements (Fig. 5A–C). Subvertical, often sheared, micro veins crosscut the cemented fault rocks.

Porosity and matrix permeability

A schematic geologic section showing the internal structure of the normal faults is presented in Fig. 6A. In this

figure, both fault core and damage zone are divided into two different parts: the fault core of uncemented and cemented fault rocks, and the damage zone of pulverized and fractured rocks. The diagram also includes the results of our porosity, ϕ , and Klinkenberg permeability, k , measurements of the samples as a function of their relative structural position (Fig. 6B,C, respectively).

The porosity of the host rock is low (0.8%), and increases in the damage zone within the fractured host rocks with distance from the fault core. This correlation is shown in Fig. 6B which, however, does not include the variations occurring in the damage zone because of small faults and meso-scale fractures. Moreover, the data shown in Fig. 6B represent only the low porosity values of the damage zone because values for the pulverized carbonate rocks are missing. As these rocks are crosscut by cataclastic shear bands, which are common features in clastic rocks with porosity higher than 15% (Antonellini *et al.* 1994; Antonellini & Aydin 1994), we project the ϕ increments in the damage zone up to this value (dashed line in Fig. 6B). It is inferred that the permeability of the pulverized carbonate rocks is higher than that of the fractured rocks of the damage zone (Fig. 6C). Within the fault footwall, the porosity decreases in the fault core and eventually collapses to 0.6% near the main slip surfaces. Although the contact between cemented and uncemented fault rocks is shown as sudden and abrupt in Fig. 6A, at micro-scale it is often gradational.

The CMS-300 automated core measurement system was used for permeability determinations at P_c of 5.5 MPa, above which the fault rocks are insensitive to pressure (cf. Rock physics section). The results of these measurements show the low permeability of the platform carbonate host

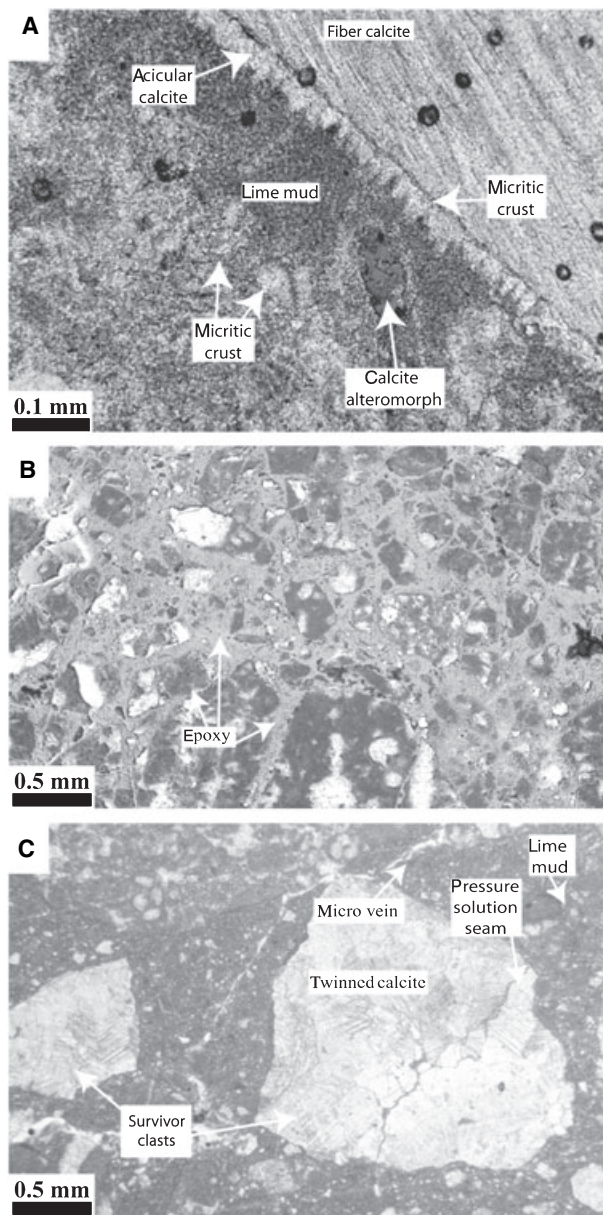


Fig. 4. (A) Photomicrographs of platform carbonate host rock, (B) fractured host rock, and (C) uncemented fault rock samples under polarized light.

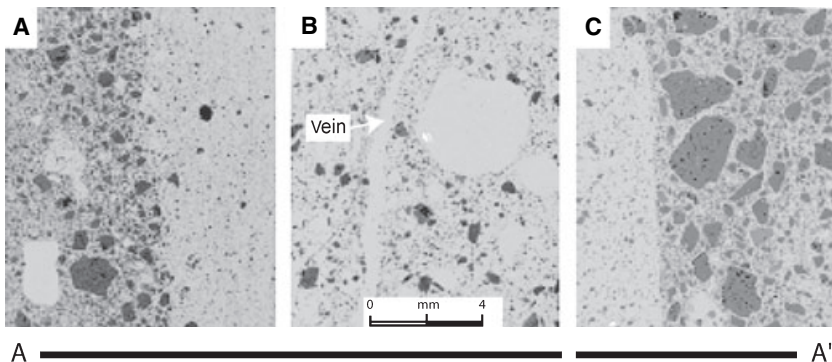


Fig. 5. (A–C) Photomicrographs of three thin-sections of the cemented fault rock under polarized light. See Fig. 3C for the location of the line A–A'.

rock ($6.77 \times 10^{-19} \text{ m}^2$), and the presence of higher permeability rocks in the damage zone of the faults (Fig. 6C). The permeabilities of the two uncemented fault rock samples are $1.35 \times 10^{-16} \text{ m}^2$ (UFR1) and $1.16 \times 10^{-16} \text{ m}^2$ (UFR2). The permeabilities of the fractured host rock samples varies between $7.72 \times 10^{-14} \text{ m}^2$ (FHR1) and $1.45 \times 10^{-17} \text{ m}^2$ (FHR4). The permeability of the pulverized host rocks is inferred to be higher than those of the fractured host rocks (dashed line in Fig. 6C). The permeability of both cemented fault rock samples is lower than the lower bound of the instrument ($9.67 \times 10^{-20} \text{ m}^2$, Fig. 6C).

Rock physics

We studied the P-wave velocity of the nine samples under increasing confining pressure. The V_p – P_c relationship is indicative of both pore geometry (sub-spherical, stiff pores versus elongated soft pores) and amount of porosity (Fig. 7A). The V_p of the cemented fault rock samples increases slightly during the first increments of pressure ($P_c \sim 5 \text{ MPa}$) and plateaus at approximately 6.6 km sec^{-1} , which is higher than the approximately 6.45 km sec^{-1} velocity plateau of the platform carbonate host rock (Fig. 7B). This higher V_p is consistent with the lower porosity of the cemented fault rocks relative to the host rock, and also with the presence of survivor dolomitic clasts in the former rocks. The V_p value of approximately 6.13 km sec^{-1} of the host rock at room pressure is similar to what Anselmetti & Eberli (1993) reported for the platform carbonates of the nearby Maiella Mountain, central Italy, and matches with the velocity range for calcite (Mavko *et al.* 1998).

The V_p of the uncemented fault rocks increases slightly during the increments of pressure and then plateaus at 5.95 – 6.2 km sec^{-1} and $P_c \sim 5 \text{ MPa}$ of pressure (Fig. 7B). On the contrary, V_p rises significantly during the first increments of pressure in the fractured host rock samples, and plateaus at 6.05 – 6.25 km sec^{-1} and $P_c \sim 10 \text{ MPa}$ (Fig. 7B). The V_s data give similar results for the nine sam-

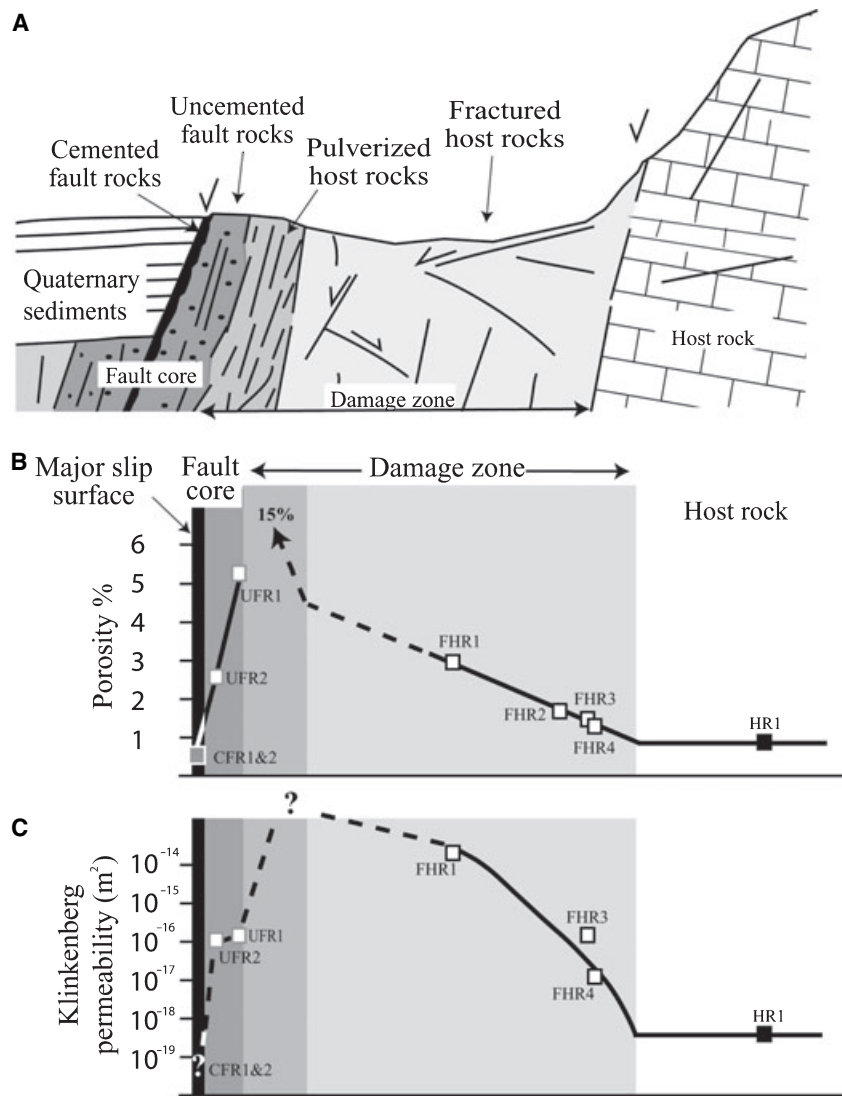


Fig. 6. (A) Geologic section showing the fault architecture and the corresponding measured porosity (B) and Klinkenberg permeability (C) of the nine samples. The 15% porosity of the pulverized host rock is inferred from the work of Antonellini & Aydin (1994) and Antonellini *et al.* (1994). The permeability of the two cemented fault rocks samples, CFR1 and CFR2, is less than $1 \times 10^{-20} \text{ m}^2$, which is the instrumental lower bound.

ples studied and are shown in Table 1 together with the computed elastic moduli for the nine samples.

Capillary pressure and pore size distribution

A mercury injection analysis was performed on cuttings of the two uncemented fault rock hand specimens using MicromeriticsTM Auto Pore III 9420 instrumentation to calculate capillary pressure. Cuttings of the two samples were first dried in a low temperature oven, and then injected with high-pressure mercury. During capillary pressure testing, the volume of mercury injected, monitored at 118 points from 11.3 to $4.06 \times 10^5 \text{ MPa}$, was corrected for closure (i.e., mercury conformance to the sample surface). These data are used to estimate the resistance of a rock to invasion by a non-wetting fluid, such as gas and most oils, by measuring the breakthrough pressure (Sneider *et al.*

1997). In this study, we determine the breakthrough pressure by picking the mercury–air capillary pressure that corresponds to 10% of the cumulative intruded mercury (90% wetting phase saturation, Schowalter 1979). This pressure, which is 349 MPa for sample UFR1 and 25.5 MPa for sample UFR2, can be used to estimate the sealing capacity of the uncemented fault rocks. A composite plot of the drainage data represents the mercury–air capillary pressure as function of the cumulative percent intruded mercury up to a maximum applied $4.06 \times 10^5 \text{ MPa}$ (Fig. 8).

We also use the results of mercury-injection capillary analysis to compute the pore radii distribution within the two uncemented fault rock samples (Fig. 9). The sample UFR1 is characterized by one main peak, which corresponds to a pore radius of $0.33 \mu\text{m}$, whereas the sample UFR2 by two main peaks that correspond to the pore radii of 0.27 and $29 \mu\text{m}$, respectively. The higher pore radius is

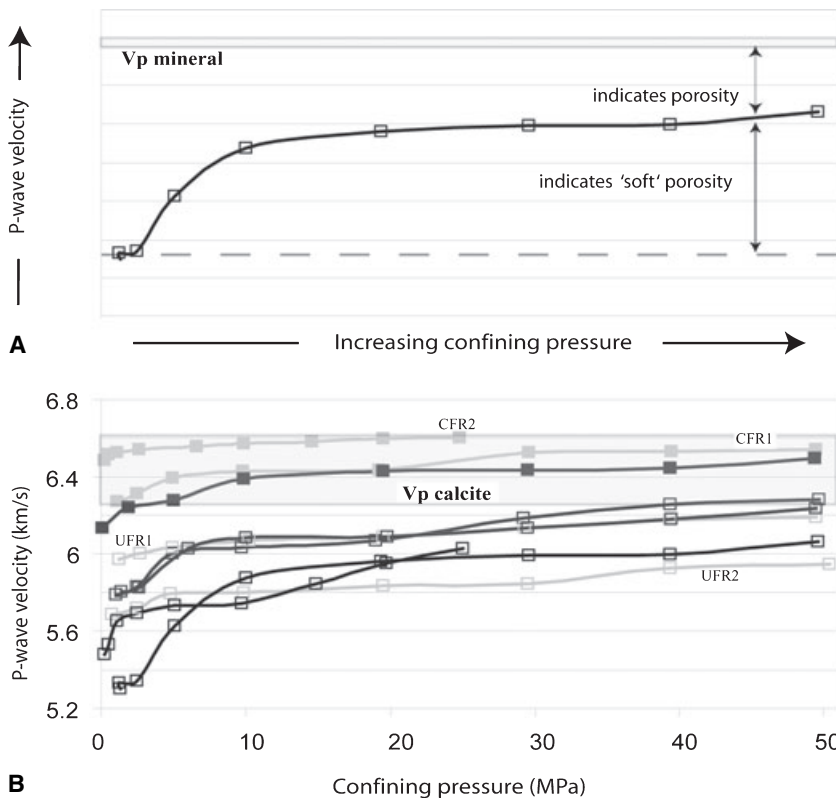


Fig. 7. (A) Idealized plot of P-wave velocity-confining pressure relation for a monomineralic rock made up of calcite, and (B) P-wave velocity-confining pressure relation for the nine samples. The sample locations are shown in Fig. 2. The shaded area in Fig. 7B represents published values for calcite (Mavko *et al.* 1998).

due to the vugs and microcracks present in the analyzed cuttings that increase the porosity of the rock up to 8.4%. For this reason, we consider the radius of $0.27 \mu\text{m}$ as representative of the pores of this sample.

DISCUSSION

We use the laboratory results to assess the pore structure, textural anisotropy, and sealing potential of the rock types that comprise the normal fault zones. We use the V_p - P_c relation to define the pore aspect ratio, the V_p - ϕ to characterize the pore type, the V_p - P_c of fault rock plugs drilled either parallel or orthogonal to the major slip surfaces to determine the textural anisotropy, and the breakthrough pressure to calculate the sealing potential of the uncemented fault rocks. Finally, we use these properties to investigate the potential role that normal faults play in the subsurface fluid flow in platform carbonates. We model the core and damage zones of the faults as granular and elastic cracked medium, respectively, and compute their matrix permeability by using the Kozeny-Carmen and Budiansky-O'Connell correlations.

Pore geometry and type

The different velocity slopes of the nine samples during cycles of pressure are indicative of the pore geometry of

the rocks (cf. Fig. 7A). As the confining pressure increases, V_p plateaus at low values of P_c (approximately 5 MPa) in both host and fault rock samples, and at high P_c values (approximately 10 MPa) in the fractured host rocks (cf. Fig. 7B). These different responses are due to differently shaped pores. The insensitivity of V_p to pressure in host and fault rocks shows that they comprise a rigid, 'stiff' frame of pores with low aspect ratio (i.e., subspherical shape). Conversely, the velocity variations in the fractured host rocks imply a 'soft' pore structure, with pores more sensitive to increments of pressure because of their high aspect ratio (i.e., elongated, crack-like shape).

The effect of porosity on the P-wave velocity is shown in Fig. 10, which includes the Hashin-Shtrikman upper and lower bounds (HS^+ and HS^- , respectively), the best-fit curve published for the platform carbonates of Bahamas and the Maiella Mountain, central Italy (Anselmetti & Eberli 1993, 1997), and the time-average equation (Wyllie *et al.* 1956, 1958, 1963). The HS^+ and HS^- bounds represent the narrowest possible bounds on elastic moduli that we can estimate for an isotropic material knowing only the volume fractions of the constituents (Mavko *et al.* 1998). The best-fit curve predicts the P-wave velocity of platform carbonates at any given porosity. Values of V_p larger than the predicted value have been empirically attributed to the presence of molds in the carbonates, which form by selective dissolution that does not affect the elastic frame of the

Fig. 8. Composite plot of drainage data computed from mercury-injection capillary tests of the two uncemented fault rock samples, UFR1 and UFR2. A mercury-air capillary pressure corresponding to 10% of the cumulative intruded mercury is used to estimate breakthrough pressures of 50 and 3.7 psi, respectively.

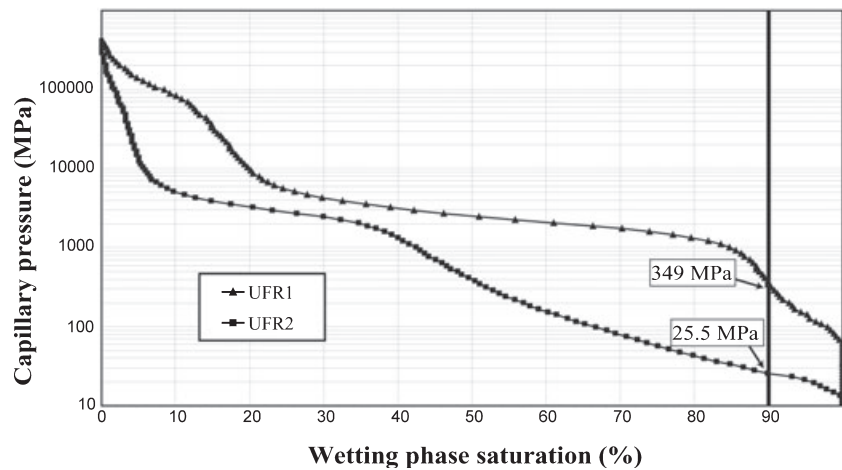
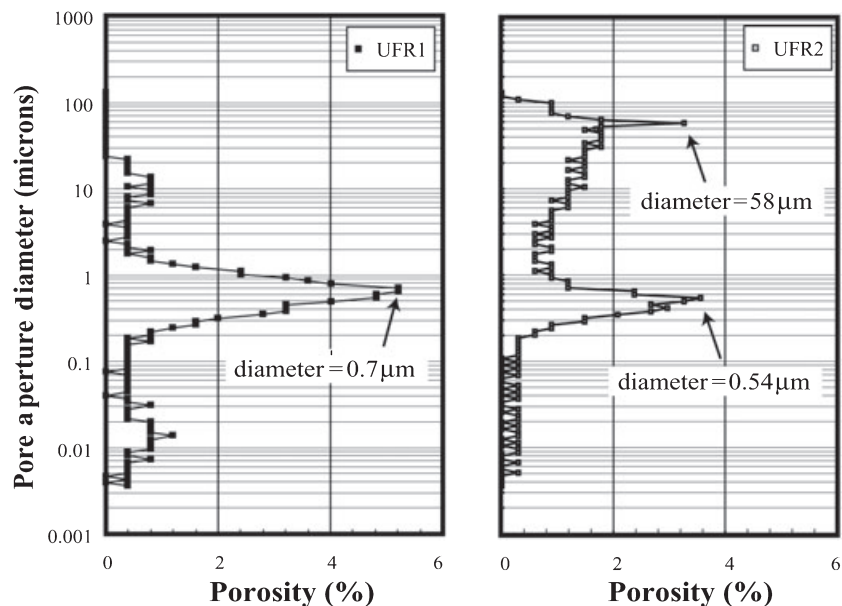


Fig. 9. Pore aperture distribution of the two uncemented fault rocks computed from capillary pressure tests. Sample UFR1 shows one main peak corresponding to a pore radius of $0.33 \mu\text{m}$. Sample UFR2 shows two peaks (0.27 and $29 \mu\text{m}$). The higher pore radius represents small vugs present in the cuttings.



rock, and thus enhance porosity but not permeability (Anselmetti & Eberli 2001). A lower V_p has been attributed to the presence of fracture/vug porosity. The time-average equation of Wyllie *et al.* (1956, 1958, 1963) relates the V_p of an isotropic, fluid-saturated, consolidated, clastic rock to its porosity; this relation is based on the fact that the total travel time can be approximated as the volume-weighted average of travel times through individual constituents of the rock.

The platform carbonate host rock data point lies on the best-fit curve. The only two data points that are close to the upper bound, HS⁺, represent the cemented fault rock samples, CFR1 and CFR2, where survivor dolomitic clasts have been documented with optical microscopy analysis. All the other data points except UFR1 are far from this bound and well below the best-fit curve, consistent with the presence of fracture and vug porosities. The three data

points above the best-fit curve line, CFR1, CFR2, and UFR1, all represent samples characterized by moldic porosity. After microscopic analysis of the samples, we conclude that the molds localize within the survivor clasts, not in the matrix and cement that form the elastic frame of the fault rock samples. Figure 10 shows that the time-average equation is not representative of the V_p - ϕ relation for carbonate rocks.

Textural anisotropy in the fault core

To determine possible velocity anisotropy caused by micro fractures within the fault rocks, we compare the V_p - P_c relations of the fault core plugs drilled with the long axes either orthogonal (CFR1 and UFR1) or parallel to the major slip surfaces (CFR2 and UFR2, Fig. 7B). The data show the contrasting response of cemented and uncement-

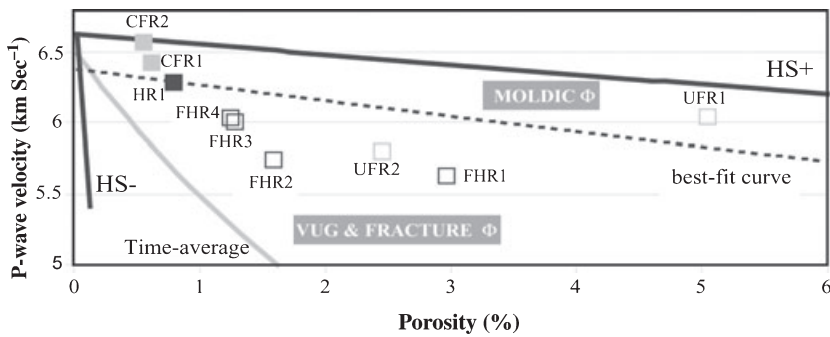


Fig. 10. Plot of velocity–porosity relations measured at 5 MPa. The thick black lines represent the Hashin–Shtrikman upper and lower bounds (HS⁺ and HS[−], respectively). The gray line represents the P-wave velocity calculated using the time-average equation (Wyllie *et al.* 1956, 1958, 1963). The dashed line represents the power law best-fit of the P-wave velocity data published by Anselmetti & Eberli (1993, 1997) for the platform-related carbonates of Bahamas and Maiella Mountain, central Italy.

ed fault rocks during increasing pressure. For the two cemented samples, the small velocity difference (ΔV_p) present at low values of P_c decreases at high pressures, due to the high velocity variation of sample CFR1 relative to CFR2. The ΔV_p variation with P_c indicates that micro fractures in the sample CFR1 are aligned along a preferential direction, sub-parallel to the major slip surfaces, and close with the increasing pressure. The micro fractures that determine this textural anisotropy effect in CFR1 are the small subvertical veins (cf. Fig. 5B). On the contrary, the constant ΔV_p (approximately 0.3 km sec^{-1}) between UFR1 and UFR2 with increasing pressure shows that micro fractures in these samples are not aligned along a preferential orientation, and thus do not cause any textural anisotropy effect.

Sealing potential of the uncemented fault rocks

The mercury-injection data are used to calculate the resistance of uncemented fault rocks to invasion by non-wetting fluids (Sneider *et al.* 1997). In terms of breakthrough pressure, which is the pressure at which non-wetting fluids can form a throughgoing flow path through the rock (Schowalter 1979), the measured pressures are 349 MPa (UFR1) and 25.5 MPa (UFR2). Based on these values, we compute the sealing capacity using representative fluid properties for both oil and gas and equations (1) and (2) presented in the Appendix (Sneider *et al.* 1997).

Input parameters used to compute the maximum sealable hydrocarbon column height are those provided by Sneider *et al.* (1997) and reported in Table 2. The two un-

cemented fault rocks show different sealing potentials, 5.7 and 77 m for gas and 10.4 and 140 m for oil for UFR2 and UFR1, respectively. According to the Sneider Seal Classification (Sneider *et al.* 1997), sample UFR1 is a Class-C seal (30–150 m oil) whereas sample UFR2 is a Class-E seal (<15 m oil). For a given breakthrough pressure, the predicted column height is higher for denser oils. The total sealing potential of the fault cores would be greater if the thin, cemented fault rocks were taken into account.

Permeability structure of the normal faults

Our petrophysical and ultrasonic analyses are consistent with a fault core with a ‘stiff’ pore structure, low ϕ and k , and a damage zone of fractured rocks with ‘soft’, crack-like pores, high ϕ and k . In order to model the permeability structure of these two main fault components, we consider the fault core as a granular medium and the damage zone as an elastic cracked medium. We assume that the fault core is composed of a bundle of straight capillary tubes of constant length and cross-sectional area, and use the Kozeny–Carmen correlation (Tiab & Donaldson 1996) to compute its bulk permeability (equation 3 in the Appendix). In order to calculate the permeability of the uncemented fault rock samples, the only samples of the fault core with a measured Klinkenberg k , we invoke effective porosities of 2.6% (UFR1, 50% moldic ϕ) and 2.5% (UFR2, no moldic ϕ) and the pore radii of $0.33 \mu\text{m}$ (UFR1) and $0.27 \mu\text{m}$ (UFR2). The calculated k is thus $3.87 \times 10^{-16} \text{ m}^2$ for sample UFR1 and $2.22 \times 10^{-16} \text{ m}^2$ for UFR2 (Table 1). These two calculated values are slightly higher than the measured Klinkenberg permeabilities. From the Kozeny–Carmen correlation, we assumed a bundle of straight tubes. If we invoke a Kozeny constant ($K_z = 2\tau$, where τ represents the tortuosity of the capillary tubes) of about 5 to represent the tortuosity of the capillary tubes, then the Klinkenberg and Kozeny–Carmen values agree. This value of Kozeny constant was reported by Carmen (1937), and transforms equation (3) into (4) in the Appendix.

Table 2 Input parameters used to calculate hydrocarbon sealing potential (from Sneider *et al.* 1997).

Input parameters	Hg/air	Gas/brine	Oil/brine
Wetting angle(θ)	140	0	0
Interfacial tension (σ) (dynes cm^{-1})	480	70	30
Brine density (g ml^{-1})		1.11	1.11
Hydrocarbon density (g ml^{-1})		0.05	0.8498

To model the fractured rock of the damage zone, we consider it an elastic cracked medium where all fractures behave as open cracks and are the main control on porosity. Assuming that fluid can flow in or out of the individual cracks in response to pressure gradients, we use the Budiansky–O’Connell correlation (Budiansky & O’Connell 1976) to calculate fracture density, ϵ , within this elastic cracked medium (equation 5 in the Appendix). Following percolation theory, we employ the calculated ϵ value in the power-law equation 6 (in the Appendix) to compute the bulk permeability of the damage zone (Zhang & Sander-son 1995). The calculated permeability values for the fractured host rocks, which range between 7.12×10^{-15} and $6.72 \times 10^{-14} \text{ m}^2$, are much larger than the measured values for all samples but FHR1.

To further analyze these data, we focus on the V_p – P_c relation again and plot the normalized P-wave velocity, V_p/V_0 (V_0 is the V_p at $P_c = 0$), of the three samples (FHR1, FHR3, and FHR4) against P_c (Fig. 11). The normalized V_p variations under increasing pressure show that FHR1 is the sample with the largest increments of velocity. The low normalized V_p variations of the FHR3 and FHR4 samples are consistent with the pores of these rocks not having elongated shapes and thus not behaving as open, slit-like cracks.

The fluid flow structure of the normal faults is thus modeled as two main units: a granular fault core, which acts as a seal for cross-fault fluid flow, and an elastic cracked medium (damage zone) that surrounds the core and forms a conduit for both cross- and along-fault fluid flow. Knowing the porosity, pore size, and elastic moduli of these fault zone components, it is possible to compute their permeability. This model does not take into account transient variation in the fault core of the along-fault permeability, nor the impact of the meso-scale structures in the damage zones on the fluid flow. Within the fault core, transient pathways evidently form along the major slip surfaces and in the nearby fault rocks due to dilation and opening of

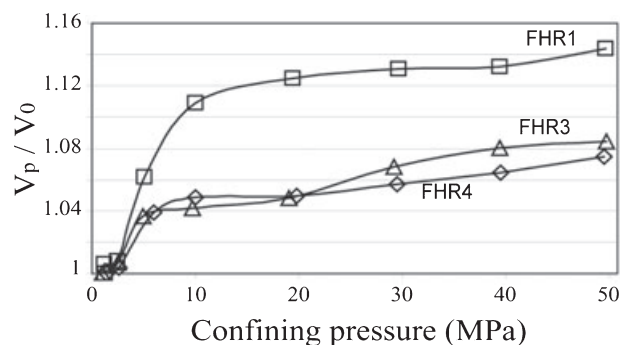


Fig. 11. Plot of normalized P-wave velocity, V_p/V_0 , of the fractured host rock samples. V_p is the P-wave velocity measured at any $P_c > 0$, V_0 that measured at $P_c = 0$.

subvertical cracks that focus diagenetic fluids. These fluids eventually coat the major slip surfaces, seal the open cracks, and cement the fault rocks (Agosta & Kirschner 2003). If associated with coseismic slip (Sibson 2000), this dilation may induce transient flow of overpressured fluids.

With respect to the damage zone, it is well known that joints, veins, and small faults made up of fragmented and brecciated rocks create pathways for fluid flow in low-porosity rocks, including platform carbonates and preexisting fault core rocks (Aydin 2000; Graham *et al.* 2005). There is evidence that sheared or opened pressure solution seams can also transport fluids (Graham *et al.* 2005). Larger, second-order faults, which include cemented fault rocks, may locally inhibit cross-fault fluid flow but enhance along-fault fluid flow within the damage zone. Thus, both porosity and permeability obtained from core-scale fractured host rock samples likely represent the minimum values at reservoir scale.

CONCLUSIONS

We studied the porosity, permeability, pore structure, textural anisotropy, and capillary pressure of carbonate rock samples collected along normal faults that border the southeastern side of the Fucino basin, central Italy. These faults juxtapose basinal continental sediments of the hangingwall with deformed platform carbonates of the footwall. The carbonate host rock is a Mesozoic boundstone made up of calcite, minor dolomite, and dark lime mud infilling the pore space. This rock, characterized by low values of porosity (0.8%) and permeability ($6.77 \times 10^{-19} \text{ m}^2$), underwent marine and burial diagenetic phases. Several sets of pressure solution seams, joints, veins, and sheared solution seams, which formed during burial diagenesis and Oligo-Pliocene contraction of the Apennines, occur throughout the platform carbonate host rocks. The fault-related samples consist of fractured carbonate host rocks from the damage zone of the faults and both matrix- and cement-supported rocks from the fault cores.

The fault cores, which include major slip surfaces, have porosity values that range from 0.6% (cemented fault rocks) to 5.2% (uncemented), and permeability values between $<9.67 \times 10^{-20} \text{ m}^2$ (cemented) and $1.35 \times 10^{-16} \text{ m}^2$ (uncemented). Small, often sheared, subvertical veins of low-Mg calcite crosscut the cemented fault rocks and induce a textural anisotropy effect on P-wave velocity. The fault damage zones are densely crosscut by several sets of opening mode (joints and veins), closing mode (pressure solution seams), and shearing mode fractures (sheared seams, sheared joints/veins, cataclastic shear bands). The samples we analyzed in the laboratory, which contain only a subset of these structures, have high values of porosity and permeability (up to 3% and $7.72 \times 10^{-14} \text{ m}^2$, respectively). However, these values rep-

resent the lower bound of damage zone properties because of the limitations in our sampling and measurements. Based on the presence of cataclastic shear bands, we infer the porosity of the pulverized carbonate rocks that flank the fault cores to be 15% or higher.

We characterized the pore structure of the rock samples by ultrasonic analysis. The pronounced velocity changes in the fractured host rock samples with increasing pressure are indicative of pores with a high aspect ratio (soft pore frame). In contrast, the insensitivity of velocity to pressure in unfractured host rocks and fault rocks indicates pores with a low aspect ratio (stiff pore frame). The velocity–porosity relations suggest that the fault rock samples have moldic porosity, whereas all the other samples have either fracture porosity (fractured host rock samples) or vug porosity (one uncemented fault rock sample). Based on this information, we calculated the permeability of the fault components, modeling the fault core as a granular medium and the damage zone as an elastic cracked medium. We used the Kozeny–Carmen correlation for the granular fault core, assigning a value of 5 to the Kozeny constant, and the Budiansky–O’Connell correlation to fractured rocks of the damage zone having large secondary porosity and high-aspect ratio pores.

The results of our laboratory analyses are consistent with normal faults forming combined barrier–conduit permeability structures for fluid flow. The fault cores act as seals for cross-fault fluid flow, compartmentalizing as much as 77 m of gas and 140 m of oil and forming Class-C seals according to the Sneider Seal classification. Conversely, the fractured damage zones form conduits for both cross-fault and along-fault fluid flow. The along-fault permeability of the cores is modulated by dilation and opening of subvertical cracks in the cemented fault rocks and along the major slip surfaces. These elements form transient pathways that focus diagenetic fluids (Agosta & Kirschner 2003), which are likely to be overpressured if the dilation and opening of cracks are associated with coseismic slip (Sibson 2000). Both faults and meso-scale fractures of the damage zone also create pathways for fluid flow in low-porosity rocks such as the platform carbonates (Aydin 2000; Graham *et al.* 2005). At aquifer and reservoir scale, these features increase the transmissibility of the damage zone and enhance both cross-fault and along-fault fluid flow. However, the effect of these structures in the overall transmissibility of the fault zones is not included in the results of our analyses because of the small size of the samples tested in the laboratory.

ACKNOWLEDGEMENTS

We acknowledge the support of both the Rock Fracture Project and Rock Physics and Borehole groups at Stanford University, and the DOE Award No. DE-FC26-

01BC15354. Thanks to Jonathan Stebbins and Karlheinz Merkle for providing us access to their laboratories, and to Jonathan Caine, Pete D’Onfro, Craig Forster, Colin Stabler, and an anonymous referee for their comments and suggestions. Part of F. Agosta’s fieldwork in central Italy was supported by a Stanford McGee grant.

REFERENCES

- Agosta F, Aydin A (2006) Deformation mechanisms and structural architecture of a normal fault in platform carbonates, Fucino basin, central Italy. *Journal of Structural Geology*, in press.
- Agosta F, Kirschner DL (2003) Fluid conduits in carbonate-hosted seismogenic normal faults of Central Italy. *Journal of Geophysical Research*, **108**. doi: 10.1029/2002JB002013.
- Anselmetti FS, Eberli GP (1993) Controls on sonic velocity in carbonates. *Pure and Applied Geophysics*, **141**, 287–323.
- Anselmetti FS, Eberli GP (1997) Sonic velocity in carbonate sediments and rocks. *Geophysical Development Series*, **6**, 53–74.
- Anselmetti FS, Eberli GP (2001) Sonic velocity in carbonates – a combined product of depositional lithology and diagenetic alterations. *Society for Sedimentary Geology Special Publication*, **70**, 193–216.
- Antonellini M, Aydin A (1994) Effect of faulting on fluid flow in porous sandstones – petrophysical properties. *American Association Petroleum Geologists Bulletin*, **78**, 355–77.
- Antonellini M, Aydin A, Pollard DD (1994) Microstructure of deformation bands in porous sandstones at Arches National Park, Utah. *Journal of Structural Geology*, **16**, 941–59.
- Aydin A (2000) Fractures, faults, and hydrocarbon entrapment, migration and flow. *Marine and Petroleum Geology*, **17**, 797–814.
- Basili A, Valensise G (1991) Contributo alla caratterizzazione della sismicità dell’area marsicano-fucense. In: *Aree Sismogenetiche e Rischio Sismico in Italia* (eds Boschi E, Basili A), pp. 197–214. ING-SGA, Rome, Italy.
- Boschi E, Guidoboni E, Ferrari G, Valensise G (1997) *Catalogo dei forti terremoti in Italia dal 461 A.C. al 1990*, 644 pp. ING-SGA, Rome, Italy.
- Bruhn RL, Parry WT, Thompson T (1994) Fracturing and hydrothermal alteration in normal fault zone. *Pure and Applied Geophysics*, **142**, 609–44.
- Budiansky B, O’Connell RJ (1976) Elastic moduli of dry and saturated cracked solids. *International Journal of Solids Structures*, **12**, 81–97.
- Caine JS, Forster CB (1999) Fault zone architecture and fluid flow – insights from field data and numerical modeling. In: *Faults and Subsurface Fluid Flow in the Shallow Crust* (eds Haneberg W, Mozley P, Moore J, Goodwin L), *American Geophysical Union Geophysical Monograph*, **133**, 101–27.
- Caine JS, Evans JP, Forster CB (1996) Fault zone architecture and permeability structure. *Geology*, **24**, 1025–8.
- Carmen PC (1937) Fluid flow through granular beds. *Transaction of the American Institute of Chemical Engineers*, **15**, 150–66.
- Cavinato GP, Carusi C, Dall’Asta M, Miccadei E, Piacentini T (2002) Sedimentary and tectonic evolution of Plio-Pleistocene alluvial and lacustrine deposits of Fucino Basin (central Italy). *Sedimentary Geology*, **148**, 29–59.
- Cello G (2000) A quantitative structural approach to the study of active faults in the Apennines (Peninsula Italy). *Journal of Geodynamics*, **29**, 265–92.

- Chester FM, Logan JM (1986) Composite planar fabric of gouge from the Punchbowl fault, California. *Journal of Structural Geology*, **9**, 621–34.
- Flodin EA, Gerdes M, Aydin A, Wiggins WD (2005) Petrophysical properties of cataclastic fault rock in sandstone. In: *Faults and Petroleum Traps* (eds Sorkhabi R, Tsuji Y), *AAPG Memoir*, **85**, 197–217.
- Galadini F, Messina P (1994) Stratigraphy of continental deposits, tectonics and Quaternary geologic evolution of the Sangro River valley, southern Abruzzi. *Bollettino della Societa' Geologica Italiana*, **3–4**, 877–92.
- Gasparini C, Iannaccone G, Scarpa R (1985) Fault-plane solutions and seismicity of the Italian peninsula. *Tectonophysics*, **117**, 59–78.
- Ghisetti F, Vezzani L (1999) Depth and modes of Pliocene–Pleistocene crustal extension of the Apennines (Italy). *Terra Nova*, **11**, 67–72.
- Ghisetti F, Kirschner DL, Vezzani L, Agosta F (2001) Stable isotope evidence for contrasting paleofluid circulation in thrust and seismogenic normal faults of central Apennines, Italy. *Journal of Geophysical Research*, **106**, 8811–25.
- Graham B, Antonellini M, Aydin A (2003) Formation and growth of normal faults in carbonates within a compressive environment. *Geology*, **31**, 11–4.
- Graham B, Girbecca R, Mesonjesi A, Aydin A (2005) Evolution of fluid pathways through fracture controlled faults in carbonates of the Albenides fold-and-thrust belt. *American Association of Petroleum Geologists Bulletin*, in press.
- Kelly YS, Peacock DCP, Sanderson DJ (1998) Linkage and evolution of conjugate strike–slip fault zones in limestones of Somerset and Northumbria. *Journal of Structural Geology*, **20**, 1477–93.
- Lucia FJ (1999) *Carbonate Reservoir Characterization*, 226 pp. Springer, New York, NY, USA.
- Mavko G, Mukerji T, Dvorkin J (1998) *The Rock Physics Handbook*, 329 pp. Cambridge University Press, Cambridge.
- Micchetti A, Brunamonte F, Serva L, Vittori E (1996) Trench investigations of the 1915 earthquake fault scarps (Abruzzo, central Italy) – geological evidence of large, historical events. *Journal of Geophysical Research*, **101**, 5921–36.
- Mollema PN, Antonellini M (1999) Development of strike–slip faults in the dolomites of the Sella Group, northern Italy. *Journal of Structural Geology*, **21**, 273–92.
- Piccardi L, Gaudemer Y, Tapponnier P, Boccaletti M (1999) Active oblique extension in the central Apennines (Italy); evidence from the Fucino region. *Geophysical Journal International*, **2**, 499–530.
- Prasad M, Nur A (2003) Velocity and attenuation anisotropy in reservoir rocks. *Expanded Abstracts of 2003 Society of Exploration Geophysics Annual Meeting*, Dallas, TX, USA (Paper RP 2–3).
- Prasad M, Palafox G, Nur A (1999) Velocity and attenuation characteristics of Daqing sandstones – effects of permeability on velocity and attenuation anisotropy. American Geophysical Union 1999 Fall Meeting. *EOS Transaction*, **80**, oral presentation #T22A-03.
- Rawling GC, Goodwin LB, Wilson JL (2001) Internal architecture, permeability structure, and hydrologic significance of contrasting fault-zone types. *Geology*, **29**, 43–46.
- Salvini F, Billi A, Wise DU (1999) Strike–slip fault-propagation cleavage in carbonate rocks; the Mattinata fault zone, Southern Apennines, Italy. *Journal of Structural Geology*, **21**, 1731–49.
- Scholz CH (1990) *The Mechanics of Earthquakes and Faulting*, 439 pp. Cambridge University Press, Cambridge.
- Schowalter TT (1979) Mechanics of secondary hydrocarbon migration and entrapment. *Geological Society of America Bulletin*, **63**, 723–60.
- Sibson RH (1977) Fault rocks and fault mechanisms. *Journal of the Geological Society of London*, **133**, 191–213.
- Sibson RH (2000) Fluid involvement in normal faulting. *Journal of Geodynamics*, **29**, 469–99.
- Sneider RM, Sneider JS, Bolger GW, Neasham JW (1997) Comparison of seal capacity determinations – core versus cuttings. *Geological Society of America Memoir*, **67**, 1–12.
- Tiab D, Donaldson E (1996) *Petrophysics – Theory and Practice of Measuring Reservoir Rock and Transport Properties*, 706 pp. Gulf Publishing Company, Geneva, AL, USA.
- Tondi E, Antonellini M, Aydin A, Marchegiani L, Cello G (2006) The role of deformation bands and pressure solution in fault development in carbonate grainstones of Majella Mountain, central Italy. *Journal of Structural Geology*, **28**, 376–391.
- Vanorio T, Prasad M, Nur A, Patella D (2002) Ultrasonic velocity measurements in volcanic rocks – correlation with microtexture. *Geophysical Journal International*, **149**, 22–36.
- Vezzani L, Ghisetti F (1998) *Carta geologica dell'Abruzzo*. S.EL.CA., Firenze.
- Wang Z (1997) Seismic properties of carbonate rocks. *Geophysical Development Series*, **6**, 29–52.
- Willemsse EJ, Peacock DC, Aydin A (1997) Nucleation and growth of strike–slip faults in limestones from Somerset, U.K. *Journal of Structural Geology*, **19**, 1461–77.
- Wyllie MRJ, Gregory AR, Gardner LW (1956) Elastic wave velocities in heterogeneous and porous medium. *Geophysics*, **21**, 41–70.
- Wyllie MRJ, Gregory AR, Gardner LW (1958) An experimental investigation of factors affecting elastic wave velocities in porous medium. *Geophysics*, **23**, 459–93.
- Wyllie MRJ, Gardner LW, Gregory AR (1963) Studies of elastic wave attenuation in porous medium. *Geophysics*, **27**, 569–89.
- Zhang X, Sanderson D (1995) Anisotropic features of geometry and permeability in fractured rock masses. *Engineering Geology*, **40**, 65–75.

APPENDIX

Calculation of sealing potential

By mercury-intrusion porosimetry (Schowalter 1979), it is possible to compute the sealing capacity of a rock sample using representative fluid properties for oil and gas and the following equations (Sneider *et al.* 1997):

$$P_{c,h/w} = \left(\frac{\sigma_{h/w} \cos \theta_{h/w}}{\sigma_{Hg/air} \cos \theta_{Hg/air}} \right) P_{c,Hg/air} \quad (1)$$

and

$$h = \frac{P_{c,h/w}}{\Delta \rho} \times 0.433 \quad (2)$$

where P_c is the capillary breakthrough pressure, h is the maximum hydrocarbon height, σ is the interfacial tension between hydrocarbon and brine, Θ is the contact angle, and $\Delta \rho$ is the difference in tension between hydrocarbon and brine. Subscripts h, w, and Hg refer, respectively, to hydrocarbon, water, and mercury. Input parameters used

to compute the maximum sealable hydrocarbon column height are those provided by Sneider *et al.* (1997) and reported in Table 2.

Calculation of matrix permeability for a granular medium

Assuming the granular medium is composed of a bundle of straight capillary tubes of constant length and cross-sectional area, the Kozeny–Carmen correlation allows the computation of permeability, k , from known porosity, ϕ , and pore radii (Tiab & Donaldson 1996). The permeability is proportional to the square of the radius of the individual tubes. By first calculating the wetted surface area per unit of pore volume, S_{vp} , and then the specific surface area of the porous material, S_{vgr} , k is calculated as:

$$k = \frac{1}{2S_{vgr}^2} \frac{\phi^3}{(1 - \phi)^2} \quad (3)$$

where 2 is the value of the Kozeny constant, K_z , reported by Tiab & Donaldson (1996). Tortuosity, τ , of the tubes is not taken into account. Considering a finite tortuosity of the capillary tubes, a value of the Kozeny constant ($K_z = 2\tau$) of about 5 was reported by Carmen (1937), which would transform our equation (3) into the most common used form of Kozeny–Carmen equation:

$$k = \frac{1}{5S_{vgr}^2} \frac{\phi^3}{(1 - \phi)^2} \quad (4)$$

Calculation of matrix permeability of an elastic cracked medium

Assuming that all fractures present in this medium behave as open cracks, are highly interconnected, and form the

main control on permeability, and that fluid flow can occur in or out of the individual cracks in response to the pressure gradients, we use the Budiansky–O’Connell correlations for elastic moduli of cracked solids to calculate the fracture density, e , and the matrix permeability of the damage zone (Budiansky & O’Connell 1976). The following relation is used to calculate the fracture density:

$$e = - \frac{K_{air}/(K_{rock} + 1)}{(16/9)(1 - \nu_{rock})/(1 - 2\nu_{rock})} \quad (5)$$

where K is the bulk modulus and ν the Poisson’s ratio. The values of K_{rock} and ν_{rock} are those computed after ultrasonic analysis at pressures of approximately 5 MPa. We also use the value of 0.149 GPa for K_{air} as reported by Mavko *et al.* (1998). Following percolation theory, we employ the calculated e value in the following power-law equation to compute permeability, k (Zhang & Sanderson 1995):

$$k = - \frac{Ap(e - dc)^{1.3}}{\pi r^2} \frac{\mu}{dh/dl} \quad (6)$$

where ‘Ap’ is the anisotropy factor, ‘dc’ the percolation threshold, r the radius of the core plugs, μ the water viscosity (0.862×10^{-3} Pa sec⁻¹ at 26.6°C), and dh/dl is the hydraulic gradient (5 MPa m⁻¹). A value of ‘dc’ is associated with each individual anisotropy factor. Thus, Ap = 1 and dc = 0.047 represent isotropic conditions, Ap = 3 and dc = 0.06 the most favorable conditions for fluid flow, and Ap = 0.33 and dc = 0.034 the least favorable.